



## Distance and size dependence of the interactions within highly ordered magnetic nanoparticle mesocrystals

Nils Neugebauer,<sup>1,2,\*</sup> Yi Wang,<sup>3</sup> Matthias T. Elm,<sup>1,2,4</sup> Detlev M. Hofmann,<sup>1,2</sup> Christian Heiliger,<sup>2,5</sup> Xingchen Ye<sup>3</sup> ,<sup>3</sup> and Peter J. Klar<sup>1,2</sup> 

<sup>1</sup>*Institute of Experimental Physics I, Justus Liebig University, Heinrich-Buff-Ring 16, 35392 Giessen, Germany*

<sup>2</sup>*Center for Materials Research (ZfM/LaMa), Justus Liebig University, Heinrich-Buff-Ring 16, 35392 Giessen, Germany*

<sup>3</sup>*Department of Chemistry, Indiana University, Bloomington, Indiana 47405, USA*

<sup>4</sup>*Institute of Physical Chemistry, Justus Liebig University, Heinrich-Buff-Ring 17, 35392 Giessen, Germany*

<sup>5</sup>*Institute for Theoretical Physics, Justus Liebig University, Heinrich-Buff-Ring 16, 35392 Giessen, Germany*



(Received 12 April 2022; revised 9 January 2023; accepted 17 April 2023; published 5 May 2023)

Arranging magnetic nanoparticles (MNPs) into highly ordered structures, so-called superlattices or mesocrystals, is of great interest from a fundamental point of view, as the employment of the corresponding coupled nanoentities introduces additional degrees of freedom to manipulate the overall magnetic characteristics of such hierarchical materials. Characterizing the associated magnetic interactions on the mesoscopic scale is indispensable for obtaining a profound understanding of the relative strengths of the types of interactions involved, such as dipole-dipole interactions, which affect the collective response of a corresponding mesocrystal. In this paper, nanoparticles are deposited onto silicon substrates by spin coating, leading to two-dimensional monolayered structures showing a close-packed hexagonal arrangement. The MNPs consist of iron oxide (magnetite  $\text{Fe}_3\text{O}_4$ ) and are coated with a nonmagnetic polymer (polystyrene). The MNPs are synthesized such that their diameters  $d_{\text{MNP}}$  are tuned in a range between 9 and 18 nm. A precise manipulation of the shell thickness  $d_{\text{shell}}$  is achieved by coating the MNPs with polystyrene of different molecular weights. In this fashion, the spacing between the MNPs,  $d_{\text{spacer}} = 2d_{\text{shell}}$ , is varied in a range between 6 and 14 nm. Within the investigated  $d_{\text{spacer}}$  range, dipolar interactions govern the collective properties showing distinct distance-dependent characteristics. As  $d_{\text{spacer}}$  increases, the dipolar coupling strength between the MNPs decreases, as deduced from the spectral features of ferromagnetic resonance experiments. These observations are further corroborated by numerical simulations of the dynamic properties of appropriate model systems. A comparison of the experimental and theoretical findings shows that material parameters, such as the magnetization  $M_{\text{MNP}}$  and the magnetocrystalline anisotropy  $C_{\text{MNP}}$  of the MNPs, are reduced compared to their bulk values.

DOI: [10.1103/PhysRevB.107.184410](https://doi.org/10.1103/PhysRevB.107.184410)

### I. INTRODUCTION

When arranging nanometer-sized entities of a material of well-defined shape, size, geometry, and orientation into highly ordered, periodic structures, novel macroscopic properties may arise [1–8]. These properties are not present in the bulk material, since such nanoparticle arrangements not only exhibit high order on the atomic scale, but also on the next higher hierarchical level at the mesoscopic scale [9]. One class of these hierarchical structures are the so-called mesocrystals, which are composed of nanoparticles (NPs) arranged on a superlattice [10]. Thus, the properties of the whole NP arrangement are essentially governed by the NP's characteristics, their spatial arrangement on a lattice, and the interaction between the NPs. By arranging NPs into mesocrystals that extend over macroscopic scales, it is possible to fabricate materials whose properties are determined by atomic interactions tuned by confinement on the nanoscale and the interparticle coupling between them on the mesoscale. From a scientific

point of view, such structures are of great interest as they offer knobs on different length scales for a precise tuning of the interactions in order to adjust the overall magnetic response according to the needs of an application. As the volume of the nanometer-sized entities that form the mesocrystal decreases, surface effects and exchange interactions become increasingly important, while the influence of dipole interactions decreases [11]. Furthermore, at sizes, which are comparable to or smaller than the typical interaction lengths in corresponding bulk materials, deviations of the associated material parameters may arise.

Magnetic mesocrystals are often called magnonic crystals, when the wavelength of a magnon (the quantized spin wave) is comparable to the periodicity of the mesocrystal. A variety of phenomena has been observed in one- [12–14] and two-dimensional magnonic crystals [13–19], such as the formation of magnonic bands with tunable band gaps that depend on the specific materials and geometries used [20]. Magnetic mesocrystals composed of magnetic nanoparticles (MNPs) are recently in the focus of interest for several reasons. First, the synthesis of MNPs has reached a level of precision which enables fabricating ensembles of well-defined MNPs with

\*nils.neugebauer@physik.uni-giessen.de

narrow size distributions. Second, the employment of MNPs may offer the opportunity to extend the investigation of confined magnons to the third spatial dimension [13,20,21].

The dynamic magnetic properties of magnonic crystals are very sensitive to the underlying periodicity, because the properties of the nanoentities vary with their size on the nanoscale, while the interaction between them depends on their spacing. Experimental investigations concerning the size-dependent properties of MNPs in nonordered systems have been performed in the past, indicating that the interaction inside MNPs of a certain size is indeed dominated by exchange interactions [22,23]. Those authors interpreted their findings on the basis of excited spin waves inside the MNPs, which are very sensitive to the size of the MNPs. The impact of the MNP size on the spin waves has been investigated theoretically by a number of researchers [11,24,25].

As the collective properties of the mesocrystal arise from the mutual interaction between neighboring MNPs, the spacing between them also has a significant impact on the macroscopic properties [26–28]. A systematic characterization of distance-dependent interactions between MNPs, such as dipolar coupling, can be performed by varying the spacing between the MNPs in a controlled way and investigating the magnetic response associated with the collective dynamic properties of the mesocrystal as a whole. Most investigations of distance-dependent properties are performed by (zero-) field-cooled magnetization measurements on both ordered and randomly arranged MNP structures investigating the real part [direct current (dc)] of the susceptibility [29–33] or the very low imaginary part [alternating current (ac)] of the susceptibility [34]. Such studies only allow a characterization of the predominantly static properties of MNPs, e.g., of the saturation magnetization  $M_{\text{MNP}}$  of the MNPs, but dynamic properties such as the propagation of spin waves and the magnetocrystalline anisotropy  $C_{\text{MNP}}$  cannot be assessed. Dynamic properties are accessible, e.g., by ferromagnetic resonance (FMR) experiments where the excitation of the magnetic material by microwaves is tuned by an external magnetic field. So far, only a few studies have used FMR for analyzing the size- and spacing-dependent properties of MNPs and MNP ensembles [28,35,36].

The investigation presented in this paper contributes to a more profound understanding of the collective dynamic properties of magnetic mesocrystals focusing on the dipolar coupling between the MNPs. Mesocrystals of defined lattice constants  $a_{\text{meso}} = d_{\text{MNP}} + d_{\text{spacer}} = d_{\text{MNP}} + 2d_{\text{shell}}$  are investigated. For this purpose, MNPs with different MNP diameters  $d_{\text{MNP}}$  and shell thicknesses  $d_{\text{shell}} = d_{\text{spacer}}/2$  are synthesized and arranged in close hexagonal monolayer packings. The dipolar interactions within such mesocrystals can be characterized by performing FMR experiments on a series of such samples where  $d_{\text{MNP}}$  and  $d_{\text{spacer}}$  are varied systematically. The experimental findings reveal a distinct dependence on both  $d_{\text{MNP}}$  and  $d_{\text{spacer}}$ . By comparing the spectral characteristics of the MNP mesocrystals with theoretical results obtained from appropriate model systems, it can be concluded that the magnetization  $M_{\text{MNP}}$  as well as the effective magnetocrystalline anisotropy  $C_{\text{MNP}}$  of the MNPs are significantly reduced compared with their bulk counterpart  $M_{\text{bulk}}$  and  $C_{\text{bulk}}$ . These effects are reflected in the values of the external magnetic

TABLE I. Overview of the sample sets investigated. Each set has been synthesized with defined MNP diameter  $d_{\text{MNP}}$  and shell thicknesses  $d_{\text{shell}}$  yielding hexagonal mesocrystals with different lattice constants of the mesocrystal  $a_{\text{meso}} = d_{\text{MNP}} + d_{\text{spacer}} = d_{\text{MNP}} + 2d_{\text{shell}}$ .

Sample set	No.	$d_{\text{MNP}}$ (nm)	$a_{\text{meso}}$ (nm)	$d_{\text{spacer}}$ (nm)
1	1-1		$15.1 \pm 0.9$	$6.1 \pm 0.5$
	1-2		$16.1 \pm 0.8$	$7.1 \pm 0.4$
	1-3	$9.0 \pm 0.5$	$16.9 \pm 1.8$	$7.9 \pm 0.6$
	1-4		$19.9 \pm 1.2$	$10.9 \pm 0.6$
	1-5		$21.7 \pm 1.0$	$12.7 \pm 0.5$
2	2-1		$20.3 \pm 1.6$	$6.1 \pm 0.8$
	2-2		$21.8 \pm 1.6$	$7.6 \pm 0.8$
	2-3	$14.2 \pm 0.9$	$22.7 \pm 1.8$	$8.5 \pm 0.9$
	2-4		$23.9 \pm 2.4$	$9.7 \pm 1.2$
	2-5		$25.7 \pm 1.7$	$11.5 \pm 0.9$
3	3-1		$24.3 \pm 1.3$	$6.1 \pm 0.7$
	3-2		$27.5 \pm 1.8$	$9.3 \pm 0.9$
	3-3	$18.2 \pm 1.2$	$28.5 \pm 2.2$	$10.3 \pm 1.1$
	3-4		$29.9 \pm 2.4$	$11.7 \pm 1.2$
	3-5		$33.1 \pm 2.8$	$14.9 \pm 1.4$

field  $B_{\text{ext}}^{\text{res}}$  at which the resonance occurs in the FMR spectrum and its linewidth  $\sigma$ . The systematic changes of the FMR spectrum on varying  $d_{\text{MNP}}$  and  $d_{\text{spacer}}$  can be correlated with the interparticle interactions by simulating the FMR spectrum based on an idealized model system of the mesocrystals.

## II. METHODS

### A. Sample preparation

The magnetic nanoparticles that form the mesocrystal consist of magnetite ( $\text{Fe}_3\text{O}_4$ ) synthesized according to the method reported previously [37,38]. Three sample sets with MNP diameters of  $d_{\text{MNP}} = 9.0, 14.2,$  and  $18.2$  nm have been synthesized. Polystyrene of different molecular weight was used as a surface surfactant. The molecular weight determines the thickness of the surface surfactant shell  $d_{\text{shell}}$  and thus the spacing between the surfaces of adjacent MNPs, i.e.,  $d_{\text{spacer}} = 2d_{\text{shell}}$ , in ordered hexagonal monolayer mesocrystals [37–40]. The particles have been dispersed in toluene with an appropriate particle concentration in order to ensure a homogeneous monolayer coverage of the high-resistivity (100) Si substrate after deposition by spin coating at 1500 rpm for 45 s. The labeling of the individual samples consists of two digits, where the first digit (1–3) represents the sample set and the second (1–5) is associated with the spacer thickness as given in Table I.

Figure 1 shows a scanning electron microscope (SEM) image of MNPs of sample 3-2 together with its two-dimensional (2D) Fourier transform as inset underlining the high degree of order of the mesocrystal's nanoentities. The lattice constant of the mesocrystal  $a_{\text{meso}}$  as well as the distance between the MNPs  $d_{\text{spacer}}$  is extracted from the 2D Fourier transform by measuring the distance of the reflexes associated with the superlattice with respect to the central reflex. The extracted parameters as well as the diameter of the MNPs of each sample are summarized in Table I. All samples show a close-packed arrangement of MNPs extending up to the edges of

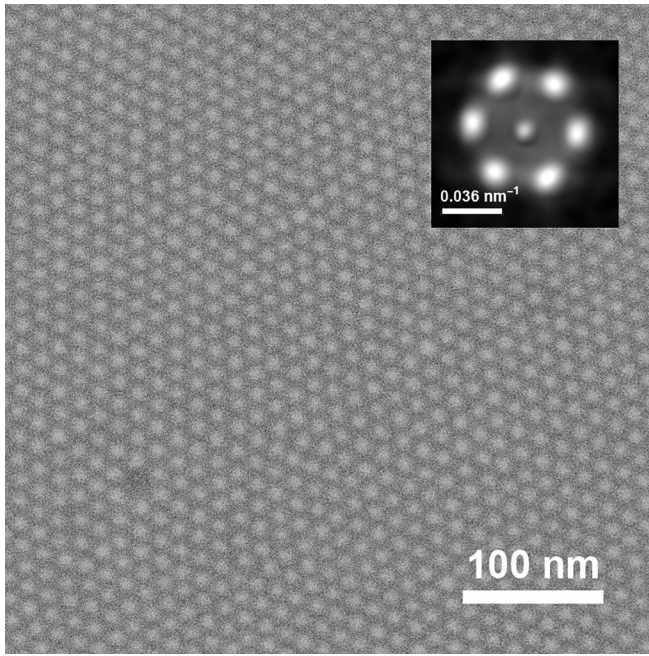


FIG. 1. SEM image of a MNP monolayer deposited by spin coating with appropriate particle concentrations and rotation speed. Inset: Corresponding Fourier transform of the SEM image, confirming the high quality of the mesocrystal and its hexagonal order.

the substrate and showing homogeneous monolayer coverage throughout, except for individually displaced MNPs. No bilayers are observed. The typical domain size of hexagonal close-packings of MNPs is 1–2  $\mu\text{m}$  for all samples.

### B. Ferromagnetic resonance setup

FMR experiments have been performed at room temperature using a Bruker ESP 300E spectrometer at  $X$ -band frequencies ( $\approx 9.8$  GHz). Good signal intensities are achieved by mounting the samples such that both the vector of the external static magnetic field  $\vec{B}_{\text{ext}}$  (pointing in the  $x$  direction) and the vector of the external excitation field caused by the microwave  $\vec{B}_\omega$  (pointing in the  $z$  direction) lie in the sample plane. This configuration yields optimal coupling of the microwave field with the sample, since the collective oscillations are excited in the direction of the magnetic easy axis of the thin film [41].

### C. Theoretical modeling approach

Simulations of the magnetic response of the sample structures using an appropriate model system are a powerful tool for evaluating and interpreting the experimental findings. We use software based on a numerical integration of the equation of motion of each magnetic moment to simulate the associated absorption spectra (corresponding to an integrated ferromagnetic resonance spectrum) of different mesocrystals. For details of the employed program code, we refer the reader to our previous publications [42,43]. Here, we consider the dipole interaction and the magnetocrystalline anisotropy only, as the collective properties of MNP mesocrystals are predominantly determined by these interactions [44–46]. In

principle, surface anisotropy effects may also have an impact on the overall characteristics. However, they play only a minor role in our samples due to the following reasons. (1) Its net contribution to the total anisotropy vanishes due to the highly spherical shape of the MNPs [47,48]. (2) The surface anisotropy only affects exchange resonance modes, but not the uniform Kittel mode, which is probed in this work [11]. (3) The strong exchange interaction across misfit dislocations within the MNPs superimposes potential surface effects [49].

Using the following simulation parameters as a starting point to describe magnetite ( $\text{Fe}_3\text{O}_4$ ), the magnetization is  $M_{\text{MNP}} = M_{\text{bulk}} = 4.8 \times 10^5$  A/m, the magnetocrystalline anisotropy constant  $C_{\text{MNP}} = C_{\text{bulk}} = -1.1 \times 10^4$  J/m<sup>3</sup>, and the empirical intrinsic damping parameter  $\alpha = 0.01$  are set to those reported for the bulk material [50]. Calculating the corresponding energies for the dipole-dipole interaction  $E_{\text{dd}}$  and magnetocrystalline anisotropy  $E_{\text{aniso}}$ , it follows that  $E_{\text{aniso}}/E_{\text{dd}}$  ranges between 0.4 and 2.5 for the investigated samples. These values are well below the critical value of  $\approx 100$  for collective behavior to occur [44,46]. Thus, in conjunction with previous investigations [45], the properties of the investigated MNP assembly are essentially collective and of a dipolar nature. A discussion of the above-mentioned simplification about the simulation approach and additional considerations about the collective behavior are given in the Supplemental Material [51]. Since we observe deviations between the theoretical modeling using the bulk material parameters and the experimental findings, the magnetization and anisotropy constant for the MNPs  $M_{\text{MNP}}$  and  $C_{\text{MNP}}$  are varied systematically between 1/8 and 1 of the bulk value in order to obtain the best agreement with the experimental FMR spectra.

To model 2D MNP monolayers, each MNP is represented by an individual point dipole. These point dipoles with a magnetic moment proportional to the MNP volume are arranged in an infinitely extended monolayer of hexagonal order with the lattice constant  $a_{\text{meso}}$  reflecting the periodicity of the mesocrystal. Assuming an infinitely extended thin film, the force resulting from the external magnetic field and the dipolar interactions between MNPs acting on an individual dipole is the same for all dipoles. Thus, also the time evolution of a magnetic moment  $\vec{m}(\vec{r}, t)$  (where  $\vec{r}$  denotes the position vector and  $t$  the time) is the same for all dipoles (i.e., MNPs). Therefore, it is sufficient to simulate the oscillation of a single point dipole at the origin and to extrapolate its precessional motion  $\vec{m}_0(\vec{r}_0, t)$  to the surrounding point dipoles  $\vec{m}_i(\vec{r}_i, t)$ . The dipole field caused by the surrounding magnetic moments  $\vec{m}_i(\vec{r}_i, t)$  acting on the magnetic moment at the origin  $\vec{m}_0(\vec{r}_0, t)$  is then calculated in each time step using the corresponding position vectors  $\vec{r}_i$  of all surrounding magnetic moments and their extrapolated orientations  $\vec{m}_i(\vec{r}_i, t) = \vec{m}_0(\vec{r}_0, t)$ . As the dipole-dipole interaction decays with  $1/r^3$  (where  $r$  denotes the distance between two dipoles), the associated magnetic dipole field  $B_{\text{dd}}$  caused by the surrounding MNPs converges for  $r \rightarrow \infty$  in a 2D system, which allows a truncation of the interaction at a radius  $R_{\text{max}}$ . The corresponding radius used for the simulations presented here is  $R_{\text{max}} = 10a_{\text{meso}}$ . A validation of this estimation along with an explanation of deriving the behavior of the surrounding point dipoles  $\vec{m}_i(\vec{r}_i, t)$  from the time dependence of a central dipole  $\vec{m}_0(\vec{r}_0, t)$  is given in the Supplemental Material [51]. Varying the spacing between the



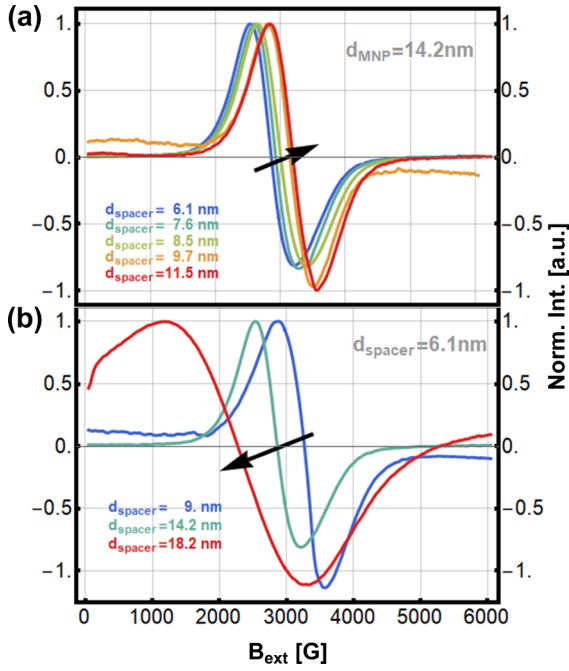


FIG. 2. (a) Measured FMR spectra of sample set 2 with MNP diameters  $d_{\text{MNP}}$  of 14.2 nm and spacing between the MNPs ranging from 6.1 to 11.5 nm. (b) Measured FMR spectra of sample S1-1, S2-1, and S3-1 with constant  $d_{\text{spacer}}$  of 6.1 nm and a variation of  $d_{\text{MNP}}$  of 9, 14.2, and 18.2 nm. The arrows indicate the changes of the resonance position  $B_{\text{ext}}^{\text{res}}$  with increasing  $d_{\text{spacer}}$  and  $d_{\text{MNP}}$  in the top and bottom graph, respectively.

point dipoles and analyzing its impact on the spectral features provides insight into the distance-dependent collective properties of the mesocrystal.

### III. RESULTS

#### A. FMR experimental results

Figure 2(a) shows five typical FMR spectra obtained from sample set 2. All mesocrystals consist of MNPs with a diam-

eter  $d_{\text{MNP}}$  of 14.2 nm. The spacing  $d_{\text{spacer}}$  between the MNPs varies from 6.1 to 11.5 nm throughout the series. Figure 2(b) depicts FMR spectra of three MNP arrangements with particle sizes  $d_{\text{MNP}}$  ranging from 9 to 18.2 nm, while keeping  $d_{\text{spacer}}$  constant at 6.1 nm. The arrows indicate the spectral changes that occur with increasing  $d_{\text{spacer}}$  and increasing  $d_{\text{MNP}}$  in Figs. 2(a) and 2(b), respectively. It is clearly visible that the spectral features depend on both  $d_{\text{spacer}}$  and  $d_{\text{MNP}}$ . Increasing  $d_{\text{spacer}}$  at constant  $d_{\text{MNP}}$  causes a shift to higher-field strengths of the external field  $B_{\text{ext}}^{\text{res}}$  at which the resonance occurs. Keeping the spacing between the MNPs constant and increasing their size, a shift of  $B_{\text{ext}}^{\text{res}}$  to lower-field strengths is observed. In addition, samples of set 3 with  $d_{\text{MNP}} = 18$  nm show a significantly larger linewidth  $\sigma$  of their FMR spectra compared to those of the samples with smaller MNP sizes of set 1 ( $d_{\text{MNP}} = 9$  nm) and 2 ( $d_{\text{MNP}} = 14$  nm), whose linewidths are approximately the same. In order to analyze the impact of  $d_{\text{spacer}}$  and  $d_{\text{MNP}}$  on the spectral features in more detail, all spectra are fitted with the derivative of a single Lorentzian curve, since only a single resonance is observed. Here we chose the following form,

$$L(B_{\text{ext}}) = \frac{A_0}{\sqrt{4\sigma^2 B_{\text{ext}}^2 + (B_{\text{ext}}^{\text{res}2} - B_{\text{ext}}^2)^2}} \quad (1)$$

and thus

$$\frac{dL}{dB_{\text{ext}}} = A_0 \frac{2B_{\text{ext}}(B_{\text{ext}}^{\text{res}2} - B_{\text{ext}}^2 - 2\sigma^2)}{[(B_{\text{ext}}^2 - B_{\text{ext}}^{\text{res}2})^2 + 4B_{\text{ext}}^2\sigma^2]^{3/2}}, \quad (2)$$

where  $A_0$  is the signal intensity,  $\sigma$  the linewidth,  $B_{\text{ext}}^{\text{res}}$  the field strength at which the resonance occurs, and  $B_{\text{ext}}$  the external field strength.

The extracted spectral parameters for each sample, i.e., the intensity  $A_0$ , the linewidth  $\sigma^{\text{expt}}$ , and the resonance field  $B_{\text{ext}}^{\text{res,expt}}$ , are summarized in Fig. 3. The lattice constant of the mesocrystal,  $a_{\text{meso}}$ , is shown on the bottom abscissa and the corresponding distance between the MNPs,  $d_{\text{spacer}}$ , on the upper abscissa. The upper panels depict the dependence of the resonance fields  $B_{\text{ext}}^{\text{res,expt}}$  on  $d_{\text{spacer}}$  for all three sample sets, while the lower panels show the dependence of the signal

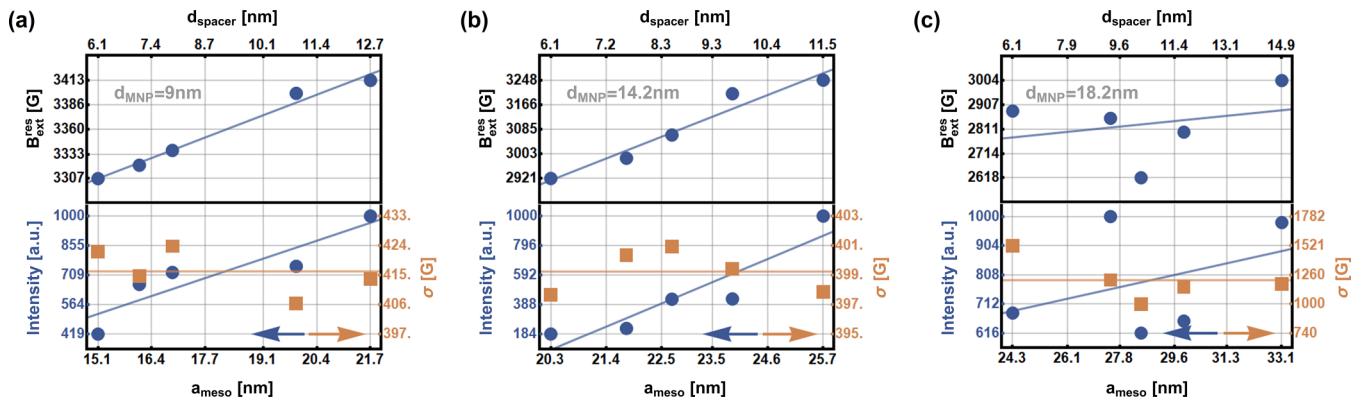


FIG. 3. Dependence of the experimentally observed resonance field  $B_{\text{ext}}^{\text{res,expt}}$ , the spectral linewidth  $\sigma^{\text{expt}}$ , and the FMR intensity on the spacing between the MNPs  $d_{\text{spacer}}$  for all three sample sets. Results from sample sets 1–3 are shown in (a)–(c), respectively. While the signal intensity and  $B_{\text{ext}}^{\text{res,expt}}$  increase with increasing  $d_{\text{spacer}}$ ,  $\sigma^{\text{expt}}$  decreases with increasing  $d_{\text{spacer}}$  for all sample sets. Colored arrows indicate the ordinate corresponding to data points of the same color. The colored straight lines are guides to the eye.

intensity (left ordinate) and the linewidth (right ordinate) on the spacing between the MNPs. The fitting confirms quantitatively the observation by visual analysis of Fig. 2 concerning the dependence on  $d_{\text{spacer}}$  for fixed  $d_{\text{MNP}}$ : (1) The experimentally observed resonance field  $B_{\text{ext}}^{\text{res,expt}}$  increases with increasing  $d_{\text{spacer}}$ , (2) the signal intensity increases with increasing  $d_{\text{spacer}}$ , and (3) the linewidth  $\sigma^{\text{expt}}$  remains unchanged with increasing  $d_{\text{spacer}}$ . Furthermore, comparing the spectral features between the different sample sets, i.e., different  $d_{\text{MNP}}$ , two more characteristics are observed: (4) The linewidths of the FMR spectra of sample set 3 are significantly larger than those of the FMR spectra of sample sets 1 and 2 and (5) the resonance field  $B_{\text{ext}}^{\text{res,expt}}$  decreases with increasing  $d_{\text{MNP}}$ .

First, we discuss the dependence of  $B_{\text{ext}}^{\text{res,expt}}$  on  $d_{\text{spacer}}$ .  $B_{\text{ext}}^{\text{res,expt}}$  is determined by the resonance condition following from the equation of motion, the Landau-Lifshitz-Gilbert equation [55]. Neglecting the damping term, Kittel has derived the resonance condition for a thin film [41]. As the demagnetizing tensor for a mesocrystal may be quite complex [56,57], but is very similar for all monolayer samples, we simplify the resonance condition as follows:

$$\begin{aligned} \frac{\omega_{\text{ext}}}{\gamma} &= \sqrt{B_{\text{tot}}(B_{\text{tot}} + \mu_0 M_{\text{film}})} \\ &= \sqrt{(B_{\text{ext}}^{\text{res}} + B_{\text{int}})(B_{\text{ext}}^{\text{res}} + B_{\text{int}} + \mu_0 M_{\text{film}})} \\ &\approx B_{\text{ext}}^{\text{res}} + B_{\text{dd}}. \end{aligned} \quad (3)$$

$\omega_{\text{ext}}$  is the angular excitation frequency of the external microwave source,  $\gamma$  is the gyromagnetic ratio of the MNPs,  $\mu_0$  the magnetic constant,  $B_{\text{ext}}^{\text{res}}$  the external magnetic field at which the resonance occurs,  $B_{\text{int}}$  accounts for additional magnetic field contributions arising internally due to local magnetic interactions between the MNPs, and  $M_{\text{film}}$  the magnetization averaged over the entire film volume. Neglecting  $M_{\text{film}}$  is justified, since in the case of MNP monolayers, it is much smaller than the magnetization  $M_{\text{MNP}}$  of spherical particles comprising it. It scales with the ratio  $d_{\text{MNP}}/d_{\text{spacer}}$  and the packing density of the MNPs. Thus,  $M_{\text{film}}$  is only  $\approx 13\%$  of  $M_{\text{MNP}}$  for sample 1-1 with  $d_{\text{MNP}} = 9$  nm and  $d_{\text{spacer}} = 6$  nm and  $M_{\text{film}} \approx 4\%$  of  $M_{\text{MNP}}$  for sample 1-5 with the same MNP diameter but a larger spacing of  $d_{\text{spacer}} = 12.7$  nm.  $B_{\text{tot}}$  is the magnetic field acting on the magnetic moment at resonance, which is a superposition of the external static field  $B_{\text{ext}}^{\text{res}}$  and the local internal field  $B_{\text{int}}$ . This internal field contribution results mainly from the dominant dipolar interaction  $B_{\text{dd}}$  between neighboring MNPs and has a minor contribution of the magnetocrystalline anisotropy field within the individual MNPs. Due to the fixed excitation frequency  $\omega_{\text{ext}}$  of the microwave,  $B_{\text{tot}}$  and thus also  $B_{\text{ext}}^{\text{res}}$  are constant. Thus,  $d_{\text{spacer}}$ -dependent properties are predominantly governed by the characteristic  $1/r^3$  dependence of  $B_{\text{dd}}$ , where  $r$  is the distance between the two dipoles. This implies that  $B_{\text{dd}}$  decreases with increasing spacer distance  $d_{\text{spacer}}$ . Consequently, the resonance fields deduced from the experiments  $B_{\text{ext}}^{\text{res,expt}}$  must increase to fulfill the resonance condition [Eq. (3)]. From the upper panels of Fig. 3, it can be concluded that  $B_{\text{ext}}^{\text{res,expt}}$  indeed increases with increasing  $d_{\text{spacer}}$  as this behavior is observed for all three sample sets.

Second, as the dipolar coupling decreases with increasing spacing  $d_{\text{spacer}}$ , demagnetization effects forcing the magnetic moments of the MNPs into the film plane become less significant, allowing them to oscillate with larger amplitudes and thus absorb more energy of the microwave field driving them externally. As a result, the intensity of the signal increases with increasing  $d_{\text{spacer}}$ .

Third, the internal damping of the precessional motion of the MNPs magnetization reflected by the linewidth parameter  $\sigma^{\text{expt}}$  does not depend on the spacing  $d_{\text{spacer}}$  between the MNPs. This suggests that the internal damping is primarily determined by the internal structure of the MNPs rather than by their mutual dipolar interaction.

Prior to analyzing the findings (4) and (5), it is necessary to discuss some general aspects of the particle synthesis. As the synthesis protocols of samples with different MNP diameters vary in terms of the reaction time and temperature [37,38], differences in the internal structure of the particles between the sample sets may occur due to different synthesis conditions. Previous investigations indicate that the magnetization of the MNPs is crucially affected by lattice imperfections within the MNPs [49]. In addition, as the size of the MNPs increases, different oxidation states of the iron ions may be observed [37], resulting in increased inhomogeneities that affect the internal damping of the magnetization oscillation.

Thus, fourth, when comparing the linewidths  $\sigma^{\text{expt}}$  of sample sets 1 and 2 with MNP diameters of  $d_{\text{MNP}} = 9$  and 14 nm, it can be seen that  $\sigma^{\text{expt}}$  is approximately constant, suggesting that the degree of internal disorder within the MNPs of diameters ranging from  $d_{\text{MNP}} = 9$  to 14 nm is quite similar. This is in good agreement with the only slightly higher synthesis temperature of 330 °C for  $d_{\text{MNP}} = 14$  nm compared with 320 °C for  $d_{\text{MNP}} = 9$  nm. Sample set 3 shows significantly wider lines, suggesting an increased internal damping. Taking into account that the degree of the MNP ordering is similar for all three sample sets, the significantly increased damping associated with a broader linewidth  $\sigma^{\text{expt}}$  for sample set 3 indicates that there is an increased internal disorder present within the MNPs of sample set 3 compared to those of sets 1 and 2. Whether the larger internal disorder of the MNPs with  $d_{\text{MNP}} = 18$  nm is due to the even higher synthesis temperature of 350 °C is not clear.

Fifth, as the diameter  $d_{\text{MNP}}$  of the MNP increases, its total magnetic moment also increases as it is proportional to the MNP volume. Thus, the dipole field  $B_{\text{dd}}$  increases with increasing  $d_{\text{MNP}}$ , resulting in a decrease of  $B_{\text{ext}}^{\text{res}}$  to fulfill the resonance condition [Eq. (3)] and the damping of the oscillation is expected to increase with increasing dipolar coupling [58].

## B. Theoretical modeling results

The results of the theoretical simulations based on the bulk magnetization of magnetite and neglecting the magnetocrystalline anisotropy are shown in Fig. 4. The simulations are performed to obtain a better understanding of the impact of dipolar interaction on the spectral features of the FMR experiments of the mesocrystals. Figure 4(a) shows modeled absorption spectra (corresponding to an integrated FMR spectrum). The magnetic moment of each MNP corresponds to a

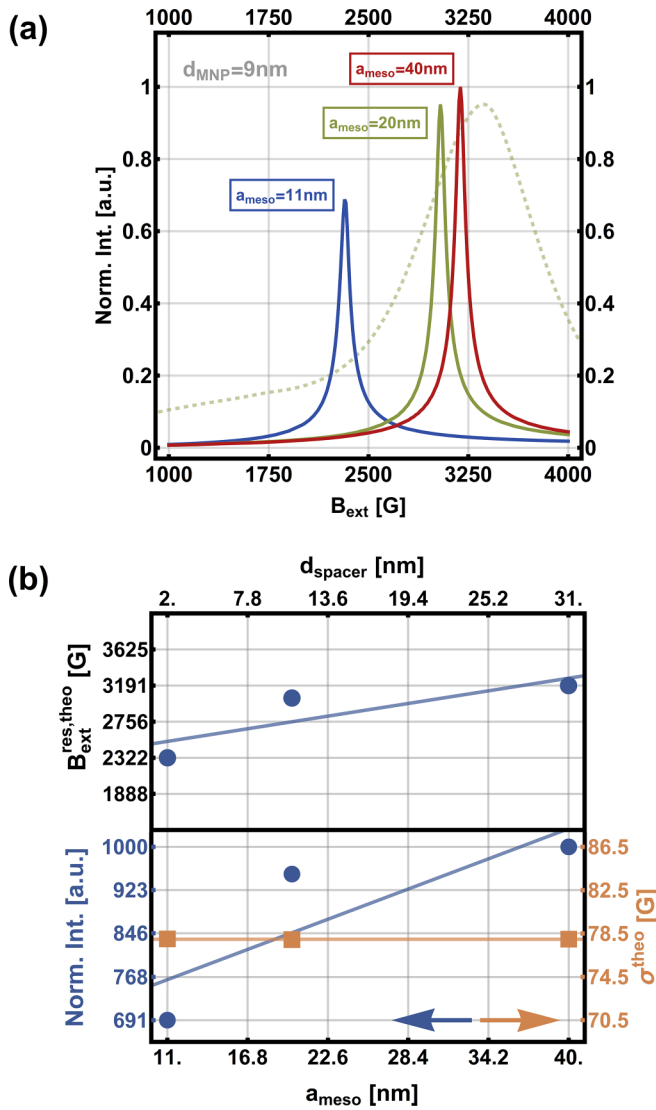


FIG. 4. (a) Measured absorption spectra (corresponding to an integrated FMR spectrum) of sample 1-4 (dashed green curve) and simulated absorption spectra (shown by continuous curves) of mesocrystals consisting of MNPs with a diameter of  $d_{\text{MNP}} = 9$  nm. Three different lattice constants are simulated ranging from  $a_{\text{meso}} = 11$  to 40 nm. (b) Corresponding line-shape parameters of the simulated spectra, such as the resonance field  $B_{\text{ext}}^{\text{res,theo}}$ , the linewidth  $\sigma^{\text{theo}}$ , and the intensity in dependence on the spacer distance  $d_{\text{spacer}}$ .

volume with a diameter of  $d_{\text{MNP}} = 9$  nm. The lattice constant of the mesocrystal is varied between  $a_{\text{meso}} = 11$  and 40 nm. The spectral parameters are extracted by fitting the calculated absorption spectra by single Lorentzian line shapes. In qualitative agreement with the experimental findings shown in Fig. 3, the extracted spectral parameters from the simulations depicted in Fig. 4(b) show that  $B_{\text{ext}}^{\text{res,theo}}$  and the signal intensity increase with increasing  $d_{\text{spacer}}$ , while the linewidth  $\sigma^{\text{theo}}$  remains almost unchanged.

However, despite good qualitative agreement of the simulations with the experiments, quantitative deviations occur. For example, the comparison of the resonance field and linewidth obtained by experiment and theory for a 2D mesocrystal of

MNPs with  $d_{\text{MNP}} = 9$  nm and  $a_{\text{meso}} = 20$  nm in Fig. 4(a) shows that the experimental spectrum (dashed green curve) is much broader than the simulated one (continuous green curve). In addition, the calculated resonance field is significantly lower than that deduced from the experiments. The same holds for all other samples. At first sight, a likely reason is the neglect of the magnetocrystalline anisotropy. However, as we will show in what follows this is not sufficient. In fact, it turns out that the material parameters, in particular of the values of the magnetization  $M_{\text{MNP}}$  and the magnetocrystalline anisotropy constant  $C_{\text{MNP}}$  of the MNPs, must be reduced with respect to the corresponding bulk values of magnetite in order to obtaining a satisfactory description of the experimental data. In order to adequately account for the magnetocrystalline anisotropy in the simulations, the random distribution of the crystal orientations of the MNPs with respect to the direction of the magnetic field has to be taken into account. For this purpose, a set of simulations with different orientations of  $B_{\text{ext}}$  with respect to the principal axis of the MNPs has been performed. In each simulation, all MNPs exhibit the same orientation of their principal axes. The resonance field  $B_{\text{ext}}^{\text{res,theo}}$  and the linewidth  $\sigma^{\text{theo}}$  in the presence of a random distribution of orientations of the MNPs can be estimated by the mean value of all resonance fields and the corresponding standard deviation of such a set of calculations. Furthermore, the calculations were not only performed for the bulk values for the magnetization  $M_{\text{bulk}}$  and magnetocrystalline anisotropy  $C_{\text{bulk}}$ , but also varied systematically assuming pairs of parameters  $M_{\text{MNP}}$  and  $C_{\text{MNP}}$ .

Figure 5(a) shows the effective resonance fields  $B_{\text{ext}}^{\text{res,theo}}$  and Fig. 5(b) the simulated effective linewidths  $\sigma^{\text{theo}}$  for a 2D mesocrystal of MNPs with  $d_{\text{MNP}} = 9$  nm and  $d_{\text{spacer}} = 11$  nm obtained by the simulations. The ratios  $M_{\text{MNP}}/M_{\text{bulk}}$  and  $C_{\text{MNP}}/C_{\text{bulk}}$  are both varied between 1/8 and 1. The values of  $B_{\text{ext}}^{\text{res,theo}}$  and  $\sigma^{\text{theo}}$  are plotted in dependence on  $M_{\text{MNP}}/M_{\text{bulk}}$  and  $C_{\text{MNP}}/C_{\text{bulk}}$  in the form of relief plots in Figs. 5(a) and 5(b). Both  $B_{\text{ext}}^{\text{res,theo}}$  and  $\sigma^{\text{theo}}$  vary in a wide range as a function of  $M_{\text{MNP}}/M_{\text{bulk}}$  and  $C_{\text{MNP}}/C_{\text{bulk}}$ . The hatched regions in both relief plots indicate where the theoretical values are in agreement with typical experimental values, i.e., those of sample 1-4 [shown in Fig. 3(a)]. The widths of the hatched regions in Figs. 5(a) and 5(b) are defined by the uncertainties of the line-shape fitting of the experimental spectrum of sample 1-4. For both quantities,  $B_{\text{ext}}^{\text{res,theo}}$  and  $\sigma^{\text{theo}}$ , there is a range of value pairs ( $M_{\text{MNP}}/M_{\text{bulk}}$  and  $C_{\text{MNP}}/C_{\text{bulk}}$ ) where the simulated values match the experiment, i.e., no decisive conclusion can be drawn from the individual relief plots. However, there is a much narrower parameter window of value pairs ( $M_{\text{MNP}}/M_{\text{bulk}}$  and  $C_{\text{MNP}}/C_{\text{bulk}}$ ) where agreement with both experimental values  $B_{\text{ext}}^{\text{res,expt}}$  and  $\sigma^{\text{expt}}$  is achieved within the experimental uncertainties. This parameter window is depicted in Fig. 5(c) as the intersection of the two hatched regions of Figs. 5(a) and 5(b). It can be concluded that a good agreement with experiment is obtained when the magnetization  $M_{\text{MNP}}$  of the MNPs is reduced to approximately 40%–60% and the anisotropy constant  $C_{\text{MNP}}$  to approximately 30%–65% with respect to their bulk values.

Similar comparisons between experiment and simulations have been carried out for a sample of set 2 with  $d_{\text{MNP}} = 14$  nm and  $d_{\text{spacer}} = 11$  nm and for a sample of set 3 with  $d_{\text{MNP}} = 18$



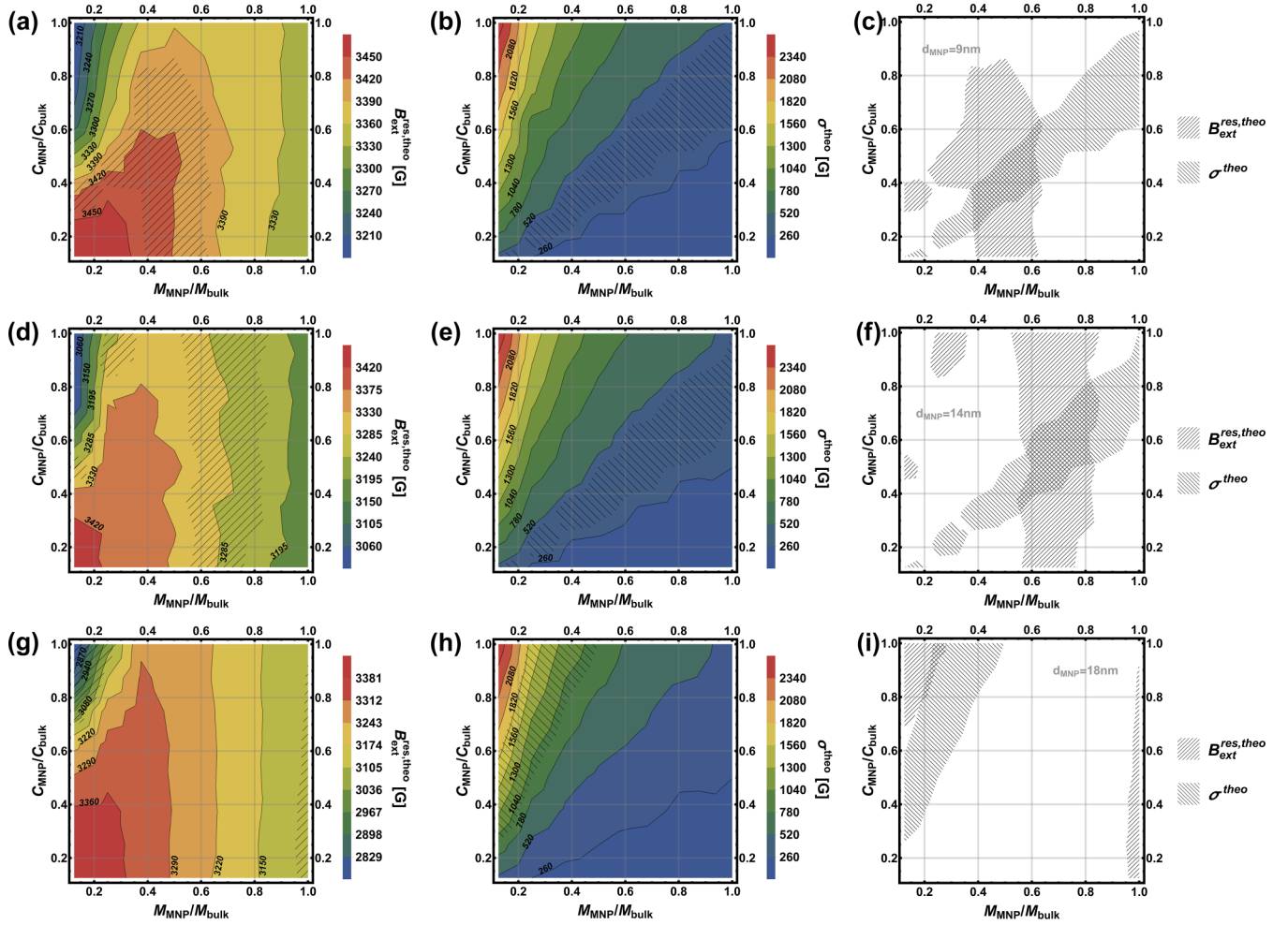


FIG. 5. (a) Effective resonance field  $B_{\text{ext}}^{\text{res,theo}}$  for different pairs  $(M_{\text{MNP}}, C_{\text{MNP}})$  of parameters for  $d_{\text{MNP}} = 9$  nm. The magnetization  $M_{\text{MNP}}/M_{\text{bulk}}$  is ranging from 1/8 to 1 and the anisotropy constant  $C_{\text{MNP}}/C_{\text{bulk}}$  is ranging from 1/8 to 1. The hatched area corresponds to pairs  $(M_{\text{MNP}}, C_{\text{MNP}})$ , which are in concordance with the experimental findings shown in Fig. 3(a) for  $d_{\text{MNP}} = 9$  nm. (b) Corresponding parameters for  $\sigma^{\text{theo}}$ . Again, the hatched area corresponds to pairs  $(M_{\text{MNP}}, C_{\text{MNP}})$ , which are in concordance with the experimental findings. (c) The intersection of the hatched areas of (a) and (b) enables an estimation of the reduced material parameters for the investigated MNPs of approximately 40%–60% for  $M_{\text{MNP}}$  and 30%–65% for  $C_{\text{MNP}}$  with respect to their bulk values. (d)–(f) depict the corresponding parameter variation of  $M_{\text{MNP}}$  and  $C_{\text{MNP}}$  for  $d_{\text{MNP}} = 14$  nm, indicating a reduction of approximately 55%–85% for  $M_{\text{MNP}}$  and 35%–80% for  $C_{\text{MNP}}$  with respect to the bulk. (g)–(i) depict the parameter variation for particles with  $d_{\text{MNP}} = 18$  nm.

nm and  $d_{\text{spacer}} = 11$  nm. The results of the former comparison are given in Figs. 5(d)–5(f) and those of the latter in Figs. 5(g)–5(i).

In the case of the sample of set 2 with  $d_{\text{MNP}} = 14$  nm, we also find a reduction of  $M_{\text{MNP}}$  and  $C_{\text{MNP}}$ , but not as pronounced as observed for the sample of set 1 with  $d_{\text{MNP}} = 9$  nm. Best agreement is obtained for a magnetization ratio  $M_{\text{MNP}}/M_{\text{bulk}}$  of approximately 55%–85% and of  $C_{\text{MNP}}/C_{\text{bulk}}$  of about 35%–80%.

In the case of the sample of set 3 with  $d_{\text{MNP}} = 18$  nm, the best agreement is obtained for a magnetization ratio  $M_{\text{MNP}}/M_{\text{bulk}}$  of approximately 20%–30% and of  $C_{\text{MNP}}/C_{\text{bulk}}$  of about 80%–100%. Although a reduction of both  $M_{\text{MNP}}/M_{\text{bulk}}$  and  $C_{\text{MNP}}/C_{\text{bulk}}$  is somewhat expected even in ideal structures, since atoms close to the surface of the MNPs are expected to behave differently than atoms close to the center of the MNP as the surface-to-volume ratio is size dependent, the results are at first sight surprising. In ideal

structures, both parameters  $M_{\text{MNP}}$  and  $C_{\text{MNP}}$  must approach the corresponding bulk values with increasing  $d_{\text{MNP}}$  and the ratios  $M_{\text{MNP}}/M_{\text{bulk}}$  and  $C_{\text{MNP}}/C_{\text{bulk}}$  should approach 1 and not decrease again as observed for the 18 nm MNPs. Thus, the observed behavior of  $M_{\text{MNP}}/M_{\text{bulk}}$  and  $C_{\text{MNP}}/C_{\text{bulk}}$  must reflect structural defects. For example, it is suggested in Ref. [49] that misfit dislocations within the individual MNPs may cause a reduction of  $M_{\text{MNP}}$  with respect to  $M_{\text{bulk}}$ .

The investigations presented here not only reproduce the findings of Ref. [49] for  $d_{\text{MNP}} = 9$  nm, but also provide additional insight into the dependence of the parameters  $M_{\text{MNP}}$  and  $C_{\text{MNP}}$  on the particle diameter  $d_{\text{MNP}}$  and deviations from structural ideality. A detailed consideration of the effect of the variation of the surface-to-volume ratio as a function of particle diameter  $d_{\text{MNP}}$  in ideal structures is given in the Supplemental Material [51]. The results for  $M_{\text{MNP}}$  and  $C_{\text{MNP}}$  for the samples with  $d_{\text{MNP}} = 9$  nm (set 1) and  $d_{\text{MNP}} = 14$  nm (set 2) are in good agreement with the anticipated dependence

on the surface-to-volume ratio, whereas the values for the MNPs with  $d_{\text{MNP}} = 18$  nm (set 3) strongly deviate from the expectation. The observed deviations for MNPs with  $d_{\text{MNP}} = 18$  nm strongly suggest increased structural differences compared with MNPs of a smaller diameter. Unfortunately, we cannot clarify the origin of the lower structural quality of the samples prepared from MNPs with diameters  $d_{\text{MNP}} > 14$  nm. Possible reasons are a higher fraction of MNPs with misfit dislocations, more point defects, i.e., iron ions of other oxidation states [37], or the onset of magnetic domain formation within the MNPs. However, we can state that accounting for dipolar interactions between the MNPs, magnetocrystalline anisotropy, and surface-to-volume ratio effects in the modeling gives a good description of ordered MNP monolayers for  $d_{\text{MNP}} \leq 14$  nm, but is not sufficient for MNP monolayers with  $d_{\text{MNP}} \geq 18$  nm.

#### IV. CONCLUSION

In summary, our results show that magnetic nanoparticles deposited into highly ordered mesocrystals exhibit a distinct dependence of their collective magnetic properties on the size of the magnetic nanoparticles and the spacing between them. This confirms that the dipolar coupling between the nanoentities on the mesoscopic scale has an impact on the macroscopic dynamic properties of the whole mesocrystalline film. Performing simulations, in which point dipoles represent

the MNPs, confirm the experimental findings. Such studies carefully conducted, from both the experimental and theoretical points of view, provide insight into deviations from the material parameters in nanoparticles with respect to the corresponding bulk material. Such studies are helpful for evaluating the internal structural quality of the employed magnetic nanoparticles and their spacing-dependent interactions and constitute important steps towards the fabrication of 3D mesocrystals out of MNPs. In particular, this holds for MNPs with  $d_{\text{MNP}} \leq 14$  nm, which only exhibit moderate effects of disorder induced by dislocations and grain boundaries. Thus, FMR in conjunction with micromagnetic simulations proves to be a powerful tool for the evaluation of MNP mesocrystals and shows distinct advantages compared to other (dc) techniques.

#### ACKNOWLEDGMENTS

We are grateful for funding in the frame of the ERDF innovation laboratory “High performance materials.” We acknowledge computational resources provided by the HPC Core Facility and the HRZ of the Justus-Liebig-University Giessen. Y.W. and X.Y. were supported by the U.S. National Science Foundation (NSF DMR-2102526). In addition, the authors thank Marcel Giar and Philipp Risius (HPC Core Facility, Justus Liebig University Giessen) for their administrative support.

- 
- [1] D. V. Talapin, E. V. Shevchenko, M. I. Bodnarchuk, X. Ye, J. Chen, and C. B. Murray, Quasicrystalline order in self-assembled binary nanoparticle superlattices, *Nature (London)* **461**, 964 (2009).
- [2] J. Chen, X. Ye, S. J. Oh, J. M. Kikkawa, C. R. Kagan, and C. B. Murray, Bistable magnetoresistance switching binary nanocrystal superlattices by in exchange-coupled  $\text{CoFe}_2\text{O}_4$ - $\text{Fe}_3\text{O}_4$  self-assembly and thermal annealing, *ACS Nano* **7**, 1478 (2013).
- [3] J. Chen, A. Dong, J. Cai, X. Ye, Y. Kang, J. M. Kikkawa, and C. B. Murray, Collective dipolar interactions in self-assembled magnetic binary nanocrystal superlattice membranes, *Nano Lett.* **10**, 5103 (2010).
- [4] D. C. Reifsnnyder, X. Ye, T. R. Gordon, C. Song, and C. B. Murray, Three-dimensional self-assembly of chalcopyrite copper indium diselenide nanocrystals into ordered films, *ACS Nano* **7**, 4307 (2013).
- [5] S. Jeong, Y. Liu, Y. Zhong, X. Zhan, Y. Li, Y. Wang, P. M. Cha, J. Chen, and X. Ye, Heterometallic seed-mediated growth of monodisperse colloidal copper nanorods with widely tunable plasmonic resonances, *Nano Lett.* **20**, 7263 (2020).
- [6] X. Ye, J. Chen, B. T. Diroll, and C. B. Murray, Tunable plasmonic coupling in self-assembled binary nanocrystal superlattices studied by correlated optical microspectroscopy and electron microscopy, *Nano Lett.* **13**, 1291 (2013).
- [7] Y. Liu, Y. Li, S. Jeong, Y. Wang, and X. Ye, Colloidal synthesis of nanohelices via bilayer lattice misfit, *J. Am. Chem. Soc.* **142**, 12777 (2020).
- [8] Y. Wang, J. Chen, Y. Zhong, S. Jeong, R. Li, and X. Ye, Structural diversity in dimension-controlled assemblies of tetrahedral gold nanocrystals, *J. Am. Chem. Soc.* **144**, 13538 (2022).
- [9] A. Fabian, M. T. Elm, D. M. Hofmann, and P. J. Klar, Hierarchical structures of magnetic nanoparticles for controlling magnetic interactions on three different length scales, *J. Appl. Phys.* **121**, 224303 (2017).
- [10] R.-Q. Song and H. Coelfen, Mesocrystals-ordered nanoparticle superstructures, *Adv. Mater.* **22**, 1301 (2010).
- [11] A. Aharoni, Effect of surface anisotropy on the exchange resonance modes, *J. Appl. Phys.* **81**, 830 (1997).
- [12] Z. K. Wang, V. L. Zhang, H. S. Lim, S. C. Ng, M. H. Kuok, S. Jain, and A. O. Adeyeye, Observation of frequency band gaps in a one-dimensional nanostructured magnonic crystal, *Appl. Phys. Lett.* **94**, 083112 (2009).
- [13] M. Krawczyk and D. Grundler, Review and prospects of magnonic crystals and devices with reprogrammable band structure, *J. Phys.: Condens. Matter* **26**, 123202 (2014).
- [14] G. Gubbiotti, S. Tacchi, M. Madami, G. Carlotti, A. O. Adeyeye, and M. Kostylev, Brillouin light scattering studies of planar metallic magnonic crystals, *J. Phys. D: Appl. Phys.* **43**, 264003 (2010).
- [15] S. Tacchi, G. Gubbiotti, M. Madami, and G. Carlotti, Brillouin light scattering studies of 2D magnonic crystals, *J. Phys.: Condens. Matter* **29**, 073001 (2017).
- [16] S. Tacchi, G. Duerr, J. W. Klos, M. Madami, S. Neusser, G. Gubbiotti, M. Krawczyk, and D. Grundler, Forbidden Band Gaps in the Spin-Wave Spectrum of a Two-Dimensional Bicomponent Magnonic Crystal, *Phys. Rev. Lett.* **109**, 137202 (2012).
- [17] F. Montoncello, S. Tacchi, L. Giovannini, M. Madami, G. Gubbiotti, G. Carlotti, E. Sirotkin, E. Ahmad, F. Y. Ogrin, and V. V. Kruglyak, Asymmetry of spin wave dispersions in



- a hexagonal magnonic crystal, *Appl. Phys. Lett.* **102**, 202411 (2013).
- [18] C. Van Opdenbosch, G. Hukic-Markosian, S. Ott, C. Abert, and M. H. Bartl, An experiment-based numerical treatment of spin wave modes in periodically porous materials, *Phys. Status Solidi B* **257**, 1900296 (2020).
- [19] N. Ross, M. Kostylev, and R. L. Stamps, Standing spin-wave mode structure and linewidth in partially disordered hexagonal arrays of perpendicularly magnetized sub-micron permalloy discs, *J. Appl. Phys.* **116**, 113909 (2014).
- [20] M. Krawczyk and H. Puzkarski, Plane-wave theory of three-dimensional magnonic crystals, *Phys. Rev. B* **77**, 054437 (2008).
- [21] S. Mamica, M. Krawczyk, M. L. Sokolovskyy, and J. Romero-Vivas, Large magnonic band gaps and spectra evolution in three-dimensional magnonic crystals based on magnetoferritin nanoparticles, *Phys. Rev. B* **86**, 144402 (2012).
- [22] P. Toneguzzo, O. Acher, G. Viau, F. Fievet-Vincent, and F. Fievet, Observations of exchange resonance modes on sub-micrometer sized ferromagnetic particles, *J. Appl. Phys.* **81**, 5546 (1997).
- [23] P. Toneguzzo, G. Viau, O. Acher, F. Fievet-Vincent, and F. Fievet, Monodisperse ferromagnetic particles for microwave applications, *Adv. Mater.* **10**, 1032 (1998).
- [24] P. A. Voltairas and C. V. Massalas, Size-dependent resonance modes in ferromagnetic spheres, *J. Magn. Magn. Mater.* **124**, 20 (1993).
- [25] R. Arias, P. Chu, and D. L. Mills, Dipole exchange spin waves and microwave response of ferromagnetic spheres, *Phys. Rev. B* **71**, 224410 (2005).
- [26] R. Arias and D. L. Mills, Theory of collective spin-wave modes of interacting ferromagnetic spheres, *Phys. Rev. B* **70**, 104425 (2004).
- [27] L. Giovannini, F. Montoncello, and F. Nizzoli, Effect of interdot coupling on spin-wave modes in nanoparticle arrays, *Phys. Rev. B* **75**, 024416 (2007).
- [28] C. Mitsumata, S. Tomita, M. Hagiwara, and K. Akamatsu, Electron magnetic resonance in interacting ferromagnetic-metal nanoparticle systems: Experiment and numerical simulation, *J. Phys.: Condens. Matter* **22**, 016005 (2010).
- [29] P. C. Rivas Rojas, P. Tancredi, O. Moscoso Londono, M. Knobel, and L. M. Socolovsky, Tuning dipolar magnetic interactions by controlling individual silicacoating of iron oxide nanoparticles, *J. Magn. Magn. Mater.* **451**, 688 (2018).
- [30] R. Voggu, N. Kumar, and C. N. R. Rao, Dependence of the properties of magnetic nanoparticles on the interparticle separation, *J. Phys. Chem. C* **112**, 17775 (2008).
- [31] C. Moya, O. Iglesias, X. Battle, and A. Labarta, Quantification of Dipolar Interactions in  $\text{Fe}_{3-x}\text{O}_4$  Nanoparticles, *J. Phys. Chem. C* **119**, 24142 (2015).
- [32] B. L. Frankamp, A. K. Boal, M. T. Tuominen, and V. M. Rotello, Direct control of the magnetic interaction between iron oxide nanoparticles through dendrimer-mediated self-assembly, *J. Am. Chem. Soc.* **127**, 9731 (2005).
- [33] G. C. Papaefthymiou, E. Devlin, A. Simopoulos, D. K. Yi, S. N. Riduan, S. S. Lee, and J. Y. Ying, Interparticle interactions in magnetic core/shell nanoarchitectures, *Phys. Rev. B* **80**, 024406 (2009).
- [34] S. Fleutot, G. L. Nealon, M. Pauly, B. P. Pichon, C. Leuvrey, M. Dillon, J. L. Gallani, D. Guillon, B. Donnio, and S. Begin-Colin, Spacing-dependent dipolar interactions in dendronized magnetic iron oxide nanoparticle 2D arrays and powders, *Nanoscale* **5**, 1507 (2013).
- [35] S. Jung, L. DeLong, J. B. Ketterson, and V. Chandrasekhar, Ferromagnetic resonance in periodic particle arrays, *Phys. Rev. B* **66**, 132401 (2002).
- [36] O. N. Martyanov, D. A. Balaev, O. V. Pylypenko, L. V. Odnodvoretz, S. V. Chernov, S. A. Nepijko, H. J. Elmers, C. M. Schneider, and G. Schönhense, FMR investigations of two-dimensional periodic arrays of disc-shaped Co particles at different temperatures, *J. Supercond. Novel Magn.* **28**, 3587 (2015).
- [37] J. Park, K. An, Y. Hwang, J. G. Park, H. J. Noh, J. Y. Kim, J. H. Park, N. M. Hwang, and T. Hyeon, Ultra-large-scale syntheses of monodisperse nanocrystal, *Nat. Mater.* **3**, 891 (2004).
- [38] Y. Wang, J. Chen, C. Zhu, B. Zhu, S. Jeong, Y. Yi, Y. Liu, J. Fiadorwu, and X. Ye, Kinetically controlled self-assembly of binary polymer-grafted nanocrystals into ordered superstructures via solvent vapor annealing, *Nano Lett.* **21**, 5053 (2021).
- [39] Y. Liu, M. Klement, Y. Wang, Y. Zhong, B. Zhu, J. Chen, M. Engel, and X. Ye, Macromolecular ligand engineering for programmable nanoprism assembly, *J. Am. Chem. Soc.* **143**, 16163 (2021).
- [40] X. Ye, C. Zhu, P. Ercius, S. N. Raja, B. He, M. R. Jones, M. R. Hauwiler, Y. Liu, T. Xu, and A. P. Alivisatos, Structural diversity in binary superlattices self-assembled from polymer-grafted nanocrystals, *Nat. Commun.* **6**, 10052 (2015).
- [41] C. Kittel, On the theory of ferromagnetic resonance absorption, *Phys. Rev.* **73**, 155 (1948).
- [42] N. Neugebauer, A. Fabian, M. T. Elm, D. M. Hofmann, M. Czerner, C. Heiliger, and P. J. Klar, Investigation of the dipole interaction in and between ordered arrangements of magnetic nanoparticles, *Phys. Rev. B* **101**, 104409 (2020).
- [43] N. Neugebauer, T. Hache, M. T. Elm, D. M. Hofmann, C. Heiliger, H. Schultheiss, and P. J. Klar, Frequency- and magnetic-field-dependent properties of ordered magnetic nanoparticle arrangements, *Phys. Rev. B* **103**, 094438 (2021).
- [44] E. H. Sanchez, M. Vasilakaki, S. Seong Lee, P. S. Normile, M. S. Andersson, R. Mathieu, A. Lopez-Ortega, B. P. Pichon, D. Peddis, C. Binns, P. Nordblad, K. Trohidou, J. Nogues, and J. A. De Toro, Crossover from individual to collective magnetism in dense nanoparticle systems: Local anisotropy versus dipolar interactions, *Small* **18**, 2106762 (2022).
- [45] J. A. De Toro, M. Vasilakaki, S. Seong Lee, M. S. Andersson, P. S. Normile, N. Yaacoub, P. Murray, E. H. Sanchez, P. Muniz, D. Peddis, R. Mathieu, K. Liu, J. Geshev, K. N. Trohidou, and J. Nogues, Remanence plots as a probe of spin disorder in magnetic nanoparticles, *Chem. Mater.* **29**, 8258 (2017).
- [46] S Mørup, Superparamagnetism and spin glass ordering in magnetic nanocomposites, *Europhys. Lett.* **28**, 671 (1994).
- [47] F. Bødker, S. Morup, and S. Linderorth, Surface Effects in Metallic Iron Nanoparticles, *Phys. Rev. Lett.* **72**, 282 (1994).
- [48] E. Lima, A. L. Brandl, A. D. Arelaro, and G. F. Goyaa, Spin disorder and magnetic anisotropy in  $\text{Fe}_3\text{O}_4$  nanoparticles, *J. Appl. Phys.* **99**, 083908 (2006).
- [49] Z. Nedelkoski, D. Kepaptsoglou, L. Lari, T. Wen, R. A. Booth, S. D. Oberdick, P. L. Galindo, Q. M. Ramasse, R. F. L. Evans, S. Majetich, and V. K. Lazarov, Origin of reduced magnetization and domain formation in small magnetite nanoparticles, *Sci. Rep.* **7**, 45997 (2017).

- [50] B. W. Zingsem, T. Feggeler, A. Terwey, S. Ghaisari, D. Spoddig, D. Faivre, R. Meckenstock, M. Farle, and M. Winklhofer, Biologically encoded magnonics, *Nat. Commun.* **10**, 4345 (2019).
- [51] See Supplemental Material at <http://link.aps.org/supplemental/10.1103/PhysRevB.107.184410> for the theoretical basis of the simulation approach used to model idealized mesocrystals, a discussion of individual versus collective behavior of MNP mesocrystals, the average film magnetization, and the dependence of the surface-to-volume ratio of the individual MNPs, which includes Refs. [41–43,50,52–55].
- [52] J. M. D. Coey, *Magnetism and Magnetic Materials* (Cambridge University Press, Cambridge, U.K., 2010).
- [53] A. Vansteenkiste, J. Leliaert, M. Dvornik, M. Helsen, F. Garcia-Sanchez, and B. van Waeyenberge, The design and verification of MuMax3, *AIP Adv.* **4**, 107133 (2014).
- [54] L. Shampine and M. Gordon, *Computer Solution of Ordinary Differential Equations: The Initial Value Problem* (Freeman, San Francisco, 1975).
- [55] R. F. L. Evans, W. J. Fan, P. Chureemart, T. A. Ostler, M. O. A. Ellis, and R. W. Chantrell, Atomistic spin model simulations of magnetic nanomaterials, *J. Phys.: Condens. Matter* **26**, 103202 (2014).
- [56] J. Kaczer and L. Murtinova, On the demagnetizing energy of periodic magnetic distributions, *Phys. Status Solidi A* **23**, 79 (1974).
- [57] H. How and C. Vittoria, Demagnetization energy and magnetic permeability tensor of spheroidal magnetic particles dispersed in cubic lattices, *Phys. Rev. B* **43**, 8094 (1991).
- [58] C. Mitumata and S. Tomita, Control of Gilbert damping using magnetic metamaterials, *Phys. Rev. B* **84**, 174421 (2011).